

# 1 Microwave spectroscopy of Q1D and Q2D organic conductors

Stephen Hill and Susumu Takahashi

Department of Physics, University of Florida, Gainesville, FL32611-8440, USA  
hill@phys.ufl.edu

This chapter reviews recent experimental studies of a novel open-orbit magnetic resonance phenomenon. The technique involves measurement of angle-dependent microwave magneto-conductivity and is, thus, closely related to the cyclotron resonance and angle-dependent magnetoresistance techniques. Data for three contrasting materials are presented:  $(\text{TMTSF})_2\text{ClO}_4$ ,  $\alpha$ - $(\text{BEDT-TTF})_2\text{KHg}(\text{SCN})_4$  and  $\kappa$ - $(\text{BEDT-TTF})_2\text{I}_3$ . These studies reveal important insights into the Fermiology of these novel materials, as well as providing access to important electronic parameters such as the in-plane Fermi velocity and quasiparticle scattering rate. It is argued that all three compounds exhibit coherent three-dimensional band transport at liquid helium temperatures, and that their low-energy magnetoelectrodynamic properties appear to be well explained on the basis of a conventional semiclassical Boltzmann approach. It is also suggested that this technique could be used to probe quasiparticles in nodal superconductors.

## 1.1 Introduction

Many of the novel broken symmetry states observed in organic conductors are driven by electronic instabilities associated with their low-dimensional Fermi surfaces (FSs), e.g. nesting instabilities [1–6]. Consequently, techniques which can probe the detailed topology of the FSs of organic charge transfer salts have been widely employed by researchers in this field (for several recent reviews, see [7–10]). Examples include: the de Haas-van Alphen (dHvA) and Shubnikov-de Haas (SdH) effects [7–12]; angle-dependent magnetoresistance oscillations (AMRO) [7–10, 13–27]; angle-resolved photoemission spectroscopy (ARPES) [28]; and cyclotron resonance (CR) [29–55]. With the exception of ARPES, all of the above techniques involve the use of strong magnetic fields and low-temperatures. In the case of the SdH and dHvA effects, the magnetic field causes Landau quantization which leads to the magneto-oscillatory behavior of various thermodynamic and transport phenomena [9, 11]. The CR and AMRO effects, meanwhile, are essentially semiclassical in origin, and are caused by the periodic motion of electrons induced by the Lorentz force [18, 21, 35, 36]. Each of these techniques requires that the product  $\omega_c\tau > 1$ , where  $\omega_c (= eB/m^*)$  is the cyclotron frequency and  $\tau$  is the

transport scattering time. Meanwhile, the SdH and dHvA effects additionally require that  $\hbar\omega_c > \{k_B T, h/\tau_\varphi\}$ , where  $\tau_\varphi$  is the quantum lifetime [11]. These criteria are easily satisfied for many organic conductors due to their exceptional purity. However, instances of the application of such methods to inorganic oxides such as the cuprate and ruthenate superconductors are extremely rare [56–58]. Consequently, ARPES is probably the technique which has been most widely applied, and has contributed most significantly to the understanding of FS driven phenomena in unconventional (including high- $T_c$ ) superconductors [59].

In this chapter, we describe a new open-orbit magnetic resonance phenomenon, the so-called periodic-orbit resonance (POR), which enables angle-resolved mapping of the in-plane Fermi velocity ( $v_F$ ) for both quasi-one-dimensional (Q1D) and quasi-two-dimensional (Q2D) organic conductors [35, 36, 47–49]. As such, this technique is complimentary to ARPES, i.e. it can provide information concerning the in-plane momentum dependence of the density-of-states ( $\propto v_F$ ) and quasiparticle scattering rate ( $\tau^{-1}$ ). However, the POR phenomenon involves measurement of the bulk microwave conductivity [60]. Consequently, it is immune to surface effects which have been known to cause problems in ARPES measurements. Furthermore, the POR technique provides sub-millivolt energy resolution and is, thus, sensitive to extremely fine details of the FS topology [35, 36, 47, 49, 55]. We will illustrate the utility of this method for several organic conductors, including  $(\text{TMTSF})_2\text{ClO}_4$  and  $(\text{BEDT-TTF})_2\text{X}$  [ $\text{X} = \text{KHg}(\text{SCN})_4$  and  $\text{I}_3$ ].

We begin by developing a theoretical framework which enables us to simulate the microwave magneto-conductance of a sample with a Q1D FS topology (see Fig. 1.1). We follow exactly the same semiclassical approach which has been adopted by various researchers to model AMRO data [18, 21]. Indeed, POR represent nothing more than an evolution of AMRO to high frequencies, such that  $\omega \sim \omega_c$  and  $\omega_c\tau > 1$ , where  $\omega$  is the measurement frequency and  $\omega_c$  represents the characteristic frequency associated with any periodic motion of quasiparticles on the FS induced by the Lorentz force. AMRO occur due to the commensurate motion of electrons on the FS for certain applied field orientations (provided  $\omega_c\tau > 1$ ). These commensurabilities affect the collective dynamical properties of the electronic system, giving rise to resistance minima (‘resonances’) when the field is aligned with real space lattice vectors. The idea of “magic angle” resonances goes back 20 years to Lebed [13], who first predicted the occurrence of angle-dependent magnetic field effects in organic conductors. Lebed’s theory predicted dimensional crossovers (3D→2D→1D) arising from commensurate electronic motion [13, 14, 26]. Some authors have since suggested that this could lead to Fermi liquid/non-Fermi liquid (FL/NFL) crossovers [61], i.e. to fundamental differences in the thermodynamic ground state at, and away from, Lebed’s “magic angles”.

When one moves to a rotating frame corresponding to incident microwave radiation of frequency  $\omega \approx \omega_c$ , one finds that the semiclassical commensurability effects discussed above occur at field orientations which depend on the frequency [27, 36, 47, 55]. In other words, there is nothing “magic” about the angles corresponding to the AMRO minima, as we will demonstrate from POR (AC AMRO) measurements presented in this chapter. Experiments also suggest that, at temperatures below 5 K and at moderate fields, the quasiparticle dynamics for all of the above mentioned compounds appear to be coherent in all three directions [47, 49, 55]. Indeed, the presented results are consistent with a 3D Fermi-liquid state, and can be easily interpreted in terms of the semiclassical Boltzmann transport equation (or an equivalent quantum mechanical theory [27, 42]). These findings are somewhat at odds with recent thermal transport measurements [62–64] presented elsewhere in this review, and do not support the idea of FL/NFL crossovers. Finally, we consider open-orbit POR in Q2D systems subjected to an in-plane magnetic field [49], and discuss the possibility of utilizing this technique to probe the normal quasiparticles in nodal superconductors [54].

## 1.2 The Periodic Orbit Resonance Phenomenon

We shall mainly limit discussion here to open-orbit POR; for detailed discussion of closed orbit POR observed in Q2D systems, refer to [35, 36]. As a starting point, we consider a Q1D system with a pair of corrugated FS sheets at  $k_x = \pm k_F$  (see Fig. 1.1(b)). Such a FS is typical for the Q1D Bechgaard salts, where electrons delocalize easily along the TMTSF cation chains due to linear stacking of the partially occupied Se  $\pi$ -orbitals [2, 4]. The FS corrugations arise from the weak orbital overlap transverse to the chain direction. Within a simple tight binding scheme, such an electronic band structure may be parameterized in terms of a set of highly anisotropic transfer integrals ( $t_a : t_b : t_c \approx 200 : 20 : 1$  meV for (TMTSF)<sub>2</sub>ClO<sub>4</sub> [4]). We begin a simple treatment of the POR phenomenon by considering an orthorhombic crystal structure, and by linearizing the  $x$ -axis dispersion about  $\epsilon_F (= 0)$  and  $k_x = \pm k_F$  (we treat a more general case below). The energy dispersion is then expressed as,

$$E(\mathbf{k}) = \hbar v_F(|k_x| - k_F) - 2t_b \cos(k_y b) - 2t_c \cos(k_z c), \quad (1.1)$$

where  $b$  and  $c$  are the  $y$  and  $z$  dimensions of the orthorhombic unit cell. The simplest case involves setting  $t_b = t_c = 0$ , in which case the FS consists of a pair of absolutely flat sheets at  $k_x = \pm k_F$  (Fig. 1.1(a)). A finite  $t_b$  results in a sinusoidal corrugation of the FS, with periodicity  $2\pi/b$  directed along the  $b$ - (or  $y$ -) axis. This situation is illustrated in Figs. 1.1(c) and (d).

We next consider the affect of the Lorentz force [ $\hbar \dot{\mathbf{k}} = -e(\mathbf{v}_F \times \mathbf{B})$ ] on a quasiparticle on the FS due to a magnetic field,  $\mathbf{B}$ , applied within the

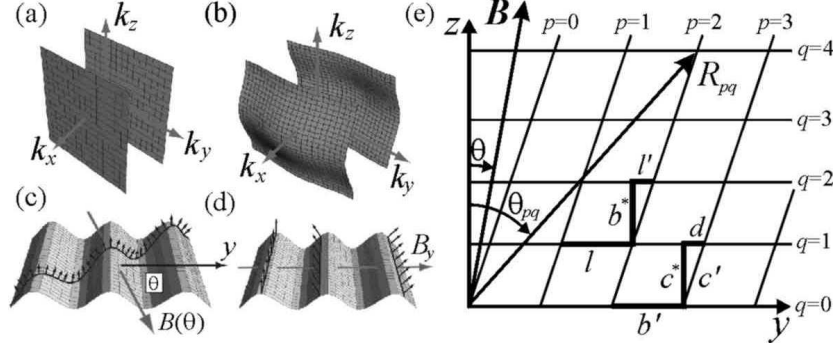


**Fig. 1.1.** Fermi surfaces corresponding to Eq. 1.1 with (a)  $t_b = t_c = 0$ , and (b) finite  $t_b$  and  $t_c$ , which causes a warping of the flat 1D FS in (a). The trajectories of quasiparticles on a warped FS (finite  $t_b$ , and  $t_c = 0$ ) are shown in (c) and (d) for different field orientations; the arrows represent the quasiparticle velocities. In (c), the field results in an oscillatory  $v_y$ , whereas this is not the case in (d), where the field is applied along the FS warping direction. (e) The oblique real-space lattice appropriate to the tight-binding model represented by Eq. 1.5. The relevant real-space vectors  $\mathbf{R}_{pq} = (0, pb' + qd, qc^*)$  for  $(\text{TMTSF})_2\text{ClO}_4$ , and  $(0, pl + ql', qb^*)$  for  $\alpha\text{-(BEDT-TTF)}_2\text{KHg(NCS)}_4$  (section 1.3.2).

$yz$ -plane (i.e. parallel to the FS). The quasiparticle follows a trajectory over the corrugated FS which is perpendicular to  $\mathbf{B}$  (Fig. 1.1(c)). For arbitrary orientation of the field within the  $yz$ -plane, this gives rise to motion which is periodic with a characteristic frequency

$$\omega_c = 2\pi \frac{\dot{k}_y}{2\pi/b} = \frac{v_F e B b}{\hbar} |\sin \theta|, \quad (1.2)$$

where  $\theta$  is the angle between the magnetic field and the corrugation axis ( $b$ -axis in this case). This periodic  $k$ -space motion has important consequences for the conductivity which, in the Boltzmann picture, is governed by the time evolution of quasiparticle velocities averaged over the FS, i.e.

$$\sigma_{ii}(\omega) \propto - \int \left( \frac{\partial f_{\mathbf{k}}}{\partial \varepsilon_{\mathbf{k}}} \right) v_i(\mathbf{k}, 0) d^3 \mathbf{k} \int_{-\infty}^0 v_i(\mathbf{k}, t) e^{-i\omega t} e^{t/\tau} dt, \quad (1.3)$$

where  $i = x, y$  or  $z$ . Naturally, the time evolution of each velocity component is governed by the field strength and its orientation. For small corrugation ( $t_b \ll t_a$ ), one can neglect variations in  $v_x$  to the first order of approximation. However, it is clear that  $v_y$  will acquire an oscillatory component with a frequency  $\omega_c$  given by Eq. 1.2. Inserting this time dependence into Eq. 1.3 results in the following expression for the  $y$ -component of the conductivity tensor:

$$\text{Re}\{\sigma_{yy}(\omega, B, \theta)\} = \frac{\sigma_o}{2} \left[ \frac{1}{1 + (\omega + \omega_c)^2 \tau^2} + \frac{1}{1 + (\omega - \omega_c)^2 \tau^2} \right], \quad (1.4)$$

where  $\sigma_o$  is the DC conductivity. This equation reduces to the simple Drude formula for the AC conductivity of a metal for  $B = 0$  (i.e.  $\omega_c = 0$ ). For finite magnetic field, Eq. 1.4 contains non-resonant and resonant terms where the  $\omega$  in the denominator of the Drude formula is replaced by  $(\omega + \omega_c)$  and  $(\omega - \omega_c)$ , respectively.

It is important to note that  $\omega$  and  $\omega_c$  essentially play identical roles in Eq. 1.4, hence the correspondence between the AMRO and POR phenomena. In a finite magnetic field, the DC conductivity  $\sigma_{yy}(\omega = 0, \theta)$  exhibits a resonance (resistance minimum) when  $\omega = \omega_c = 0$ , i.e. when the magnetic field is directed along the  $b$ -direction corresponding to a “magic angle” ( $\theta = 0$ ). From Fig. 1.1(d), it is clear that when the applied field is directed along the corrugation axis (magic angle), it has no influence on either the  $y$  or  $z$  components of the quasiparticle velocities. Consequently, the usual Drude behavior is recovered, and both  $\sigma_{yy}$  and  $\sigma_{zz}$  exhibit a maximum at  $\omega = 0$ . As the field is rotated away from the magic angle,  $\omega_c$  becomes finite and increases as  $\sin\theta$ . Consequently,  $\sigma_{yy}(\omega = 0)$  decreases ( $\rho_{yy}$  increases); the finite  $\omega_c$  essentially leads to a randomization of  $v_y$  between successive collisions and, therefore, to a suppression of  $\sigma_{yy}$ . This is the origin of the resistance minima observed in AMRO experiments (see further discussion below). For a finite  $\omega_c$  ( $\theta \neq 0$ ), meanwhile, the resonance can be recovered by setting  $\omega = \omega_c$ ; in this situation,  $v_y$  remains static in a rotating frame corresponding to the driving frequency  $\omega$ . This is the origin of the POR phenomenon [35,36], which was originally discussed by Osada et al. [18]. What one sees, therefore, is that AMRO correspond to DC conductivity resonances observed by sweeping  $\omega_c$ , while POR correspond to precisely the same resonances except that they are observed at finite  $\omega$ , i.e. the Drude conductivity peak moves away from  $\omega = 0$  to  $\omega = \omega_c$ . As we shall demonstrate, POR are also best observed by sweeping  $\omega_c$ ; this may be achieved either by varying  $B$  directly, or by rotating the field in exactly the same way as one would in an AMRO experiment. For the field rotation measurements (AC AMRO), we note that two resonances should be observed at  $\theta = \pm \sin^{-1}\{\hbar\omega/v_F e B b\}$ , not a single resonance at  $\theta = 0$ . Thus, from this semiclassical point-of-view, one clearly sees that the directions corresponding to AMRO minima are not really “magic”.

The preceding discussion assumes the existence of an extended 3D FS, i.e. that the sample under investigation exhibits coherent 3D band transport. Given the extreme anisotropy of many organic conductors, it is natural to consider what would happen if the quasiparticle dynamics were incoherent in one or more directions. A number of authors have explored this limit in which the scattering rate exceeds the hopping frequency in a given direction within a crystal [65–67], e.g.  $\tau^{-1} > t_c/\hbar$ . In this case, it is meaningless to consider energy dispersion and FS warping in this direction; essentially, the

lifetime broadening of quasiparticle states exceeds the bandwidth in that direction. McKenzie et al. have shown that, for layered materials, POR occur for both coherent and weakly incoherent interlayer transport [66]. Thus, the observation of POR does not necessarily imply the existence of a 3D FS. By weakly incoherent, it is implied that one cannot define an interlayer momentum ( $\hbar k_z$ ), but that the in-plane momentum is conserved when a quasiparticle hops between layers [65, 66]. Therefore, it is likely that many of the conclusions drawn from the POR studies described in this chapter apply regardless of whether a truly 3D FS exists. Nevertheless, we will argue that all of the materials investigated in this chapter exhibit a coherent 3D Fermi liquid state at low temperatures ( $< 5$  K).

In principle, one could also observe POR by sweeping  $\omega$ , just as one can use zero-field optical techniques to measure the Drude conductivity in a conventional metal [68]. However, the large effective masses ( $\sim 2m_e$ ) and exceptionally long scattering times (tens of ps) found in many organic conductors at liquid helium temperatures make it very difficult to observe POR using broadband techniques, due to lack of sensitivity and/or resolution at microwave frequencies [69]. Hence the need for high-sensitivity narrow-band cavity-based techniques [70–74]. As an aside, as noted above, frequency- and field-swept experiments are essentially equivalent in the Boltzmann theory. Consequently, one should be able to extract essentially the same information from a POR measurement as one would from a broadband optical measurement. We will make such comparisons in section 1.5 of this chapter.

### 1.2.1 Modification of theory for realistic crystal structures

As shown in the previous section, a finite tight-binding transfer integral along the  $y$ -direction (perpendicular to the highly conducting  $x$ -axis) results in a single resonance in the  $y$ -component of the conductivity tensor ( $\sigma_{yy}$ ) when  $\omega = \omega_c$ . In the preceding example, we set  $t_c = 0$ . Consequently,  $v_z = 0$  for all momenta, and it is trivial to show that this leads to  $\sigma_{zz} = 0$ . If  $t_c$  were finite, the FS would acquire an additional corrugation along the orthogonal  $z$ -direction. For such an orthorhombic crystal, one can show that the Lorentz force leads to completely separable solutions for  $v_y(t)$  and  $v_z(t)$  (because the corrugation axes are orthogonal). In fact,  $v_y(t) [= 2bt_b \sin\{k_y(t)b\}/\hbar]$  depends only on  $t_b$  and  $v_z(t) [= 2ct_c \sin\{k_z(t)c\}/\hbar]$  depends only on  $t_c$ . Now that  $v_z$  also oscillates, one would expect to observe a DC AMRO minimum in  $\sigma_{zz}$  when the field is directed exactly along the  $c$ -axis. At finite frequencies, this resonance would evolve into two POR at angles  $\theta' = \pm \sin^{-1}\{\hbar\omega/v_F e B c\}$  where, this time,  $\theta'$  is the angle between the applied field and the  $c$ - (or  $z$ -) axis. The important point to note here is that only  $\sigma_{zz}$  is sensitive to  $t_c$  and only  $\sigma_{yy}$  is sensitive to  $t_b$ . Thus, one would need to independently measure the conductivities along orthogonal directions in such a crystal in order to extract information about the two transverse tight-binding transfer integrals.

We note that an absolute measure of these parameters would require absolute measurements of the conductivity, which is extremely difficult using a narrow-band cavity perturbation technique [69–72]. However, as we shall now see, one can directly obtain information concerning the relative magnitudes of different transfer integrals from measurement of a single conductivity component for crystal structures with symmetry lower than orthorhombic [21,47].

We now consider the quite general case of an oblique lattice [21,47], as illustrated in Fig. 1.1(e). We also consider the possibility of electron hopping not only between nearest-neighbor chains, but also to next-nearest-neighbors and so on. In the standard fashion, we label chains by a pair of indices  $p$  and  $q$ , as illustrated in Fig. 1.1(e). For convenience, we treat the specific case of the  $(\text{TMTSF})_2\text{ClO}_4$  lattice for which the crystallographic  $a$ -axis corresponds to the chain direction,  $b'$  ( $\perp a$ ,  $\parallel ab$ -plane) corresponds to the intermediate conducting direction, and  $c^*$  ( $\perp ab$ -plane) corresponds to the least conducting direction [4]. We then reference this lattice to a Cartesian coordinate system by aligning the crystallographic  $a$  and  $b'$ -directions with the  $x$ - and  $y$ -axes, respectively. The real-space vectors  $\mathbf{R}_{pq}$  which define the locations of neighboring chains are then given by  $(0, pb' + qd, qc^*)$ , where  $p$  and  $q$  are integers and  $d$  is defined in Fig. 1.1(e). One can then write down a linearized dispersion relation about  $\epsilon_F (= 0)$  and  $k_x = \pm k_F$  in terms of a set of tight-binding transfer integrals,  $t_{pq}$ , between neighboring chains, i.e.

$$\begin{aligned} E(\mathbf{k}) &= \hbar v_F(|k_x| - k_F) - \sum_{p,q} t_{pq} \cos(\mathbf{k} \cdot \mathbf{R}_{pq}) \\ &= \hbar v_F(|k_x| - k_F) - \sum_{p,q} t_{pq} \cos[(pb' + qd)k_y + (qc^*)k_z]. \end{aligned} \quad (1.5)$$

Each transfer integral  $t_{pq}$  will produce a sinusoidal corrugation of the FS, with the corrugation axis defined by the real-space vector  $\mathbf{R}_{pq}$ , and the period given by  $2\pi/|\mathbf{R}_{pq}|$ ; the amplitudes of the corrugations will scale with  $t_{pq}$ . More importantly, each  $t_{pq}$  will produce a sinusoidal modulation of the quasi-particle velocity components transverse to the chains, and to a corresponding resonance in the conductivity [21]. However, the dispersion relation given by Eq. 1.5 does not give rise to completely separable solutions for  $v_y(t)$  and  $v_z(t)$ . In particular, hopping in the  $c$ -direction (finite  $q$ ) will have a direct influence on  $v_y(t)$ . Furthermore, diagonal hopping terms involving finite  $p$  and  $q$  will affect both velocity components and, consequently, give rise to resonances in both  $\sigma_{yy}$  and  $\sigma_{zz}$ . Thus, in general, one may now expect to observe several POR harmonics (or AMRO minima) depending on the relative magnitudes of the higher order  $t_{pq}$  transfer integrals.

In order to parameterize this more general case, one can define a set of angles,  $\theta_{pq}$ , corresponding to interchain directions [see Fig. 1.1(e)]. Then,

$$\tan \theta_{pq} = \frac{pb'}{qc^*} + \frac{d}{c^*}, \quad (1.6)$$

where this angle is referenced to the  $z$ -direction [ $c^*$ -axis for  $(\text{TMTSF})_2\text{ClO}_4$ ] within the plane of the FS ( $yz$ -plane) [47]. These are the so-called Lebedev magic angles [13]. One can then go through the same procedure as in the preceding section in order to consider the effect of an applied magnetic field. For field rotation in the plane of the FS, the characteristic POR frequencies are given by

$$\omega_{pq} = \frac{v_F e B R_{pq}}{\hbar} |\sin(\theta - \theta_{pq})| = \omega_{pq}^{max} |\sin(\theta - \theta_{pq})|, \quad (1.7)$$

where  $\theta$  is again measured relative to the  $z$ -axis, and  $\omega_{pq}^{max}$  ( $= v_F e B R_{pq} / \hbar$ ) is the maximum value of  $\omega_{pq}$  occurring when  $|\theta - \theta_{pq}| = 90^\circ$  [47]. The transverse components of the conductivity tensor ( $\sigma_{yy}$  and  $\sigma_{zz}$ ) may then be written

$$\text{Re}\{\sigma_{ii}(\omega, \theta, B)\} \propto \sum_{p,q} A_{ii}^{pq} \left[ \frac{1}{1 + (\omega + \omega_{pq})^2 \tau^2} + \frac{1}{1 + (\omega - \omega_{pq})^2 \tau^2} \right], \quad (1.8)$$

where  $A_{yy}^{pq} = \{(pb' + qd)t_{pq}\}^2$  and  $A_{zz}^{pq} = \{qc^*t_{pq}\}^2$ . From these expressions, one can see that DC AMRO minima occur when  $\theta = \theta_{pq}$  ( $\omega_{pq} = 0$ ), provided the appropriate  $A_{yy}^{pq}$  is finite. However, in general, POR will be observed when  $\omega = \omega_{pq}$ , at angles given by Eq. 1.7, i.e.

$$\theta_{POR} = \theta_{pq} \pm \sin^{-1}(\omega / \omega_{pq}^{max}). \quad (1.9)$$

Here, one again sees that the resonance condition reduces to the DC result,  $\theta = \theta_{pq}$ , when  $\omega = 0$ .

Each resonance, be it a DC AMRO minimum or a POR, corresponds to a given transfer integral,  $t_{pq}$ . As noted above, the amplitude of each POR is proportional to  $A_{ii}^{pq} \propto t_{pq}^2$ . Thus, the relative intensities of POR provide a direct measure of the Fourier spectrum of the FS warping, since the  $t_{pq}$  represent the Fourier amplitudes associated with each modulation vector  $\mathbf{R}_{pq}$  [21]. We note that DC AMRO minima for a given  $p/q$  occur at the same angles, irrespective of the values of  $p$  and  $q$ . This is not the case for a finite frequency POR measurement, where the resonance depends on both  $\theta_{pq}$  and  $R_{pq}$  through the prefactor in Eq. 1.7. Indeed, the POR condition (Eq. 1.7) defines a set of curves in the 2D  $\omega$  versus  $\theta$  plane, whereas AMRO correspond simply to the 1D line of points representing to the  $\omega = 0$  intercepts of the POR curves. The POR data presented in the following section have been performed at many different frequencies, both by sweeping the field (equivalent to sweeping  $\omega$ ) at a fixed orientation relative to the crystal, and by varying the orientation (sweeping  $\theta$ ) of a static field.

### 1.3 Experimental observation of POR for Q1D systems

In this section, we present experimental POR data obtained for two contrasting Q1D systems:  $(\text{TMTSF})_2\text{ClO}_4$  and  $\alpha$ -(BEDT-TTF) $_2\text{KHg}(\text{SCN})_4$ .



Microwave measurements were carried out using a millimeter-wave vector network analyzer and a high sensitivity cavity perturbation technique; this instrumentation is described in detail elsewhere [73,74]. In order to enable in-situ rotation of the sample relative to the applied magnetic field, two different techniques were employed. The first involved a split-pair magnet with a 7 T horizontal field and a vertical access. Smooth rotation of the entire rigid microwave probe relative to the fixed field was achieved via a room temperature stepper motor (with  $0.1^\circ$  resolution). The second method involved in-situ rotation of the end-plate of a cylindrical cavity, mounted with its axis transverse to a 17 T superconducting solenoid. Details concerning this cavity, which provides an angle resolution of  $0.18^\circ$ , have been published elsewhere [74]; a combination of the two methods enables double-axis rotation capabilities.

### 1.3.1 (TMTSF)<sub>2</sub>ClO<sub>4</sub>

(TMTSF)<sub>2</sub>ClO<sub>4</sub> undergoes a structural transition at  $T_{AO} = 24$  K which involves an ordering of the ClO<sub>4</sub> anions (which lack a center of inversion) [4]. The anion order, which results in a doubling of the unit cell along the  $b$ -direction, is extremely sensitive to the cooling rate around  $T_{AO}$ . When cooled rapidly (quenched), at rates exceeding 50 K/min, the ClO<sub>4</sub> anions remain disordered and the system undergoes a transition to a spin-density-wave (SDW) insulating ground state below 6 K. On the other hand, if the sample is cooled slowly (relaxed) through  $T_{AO}$  at a rate of less than 0.1 K/min, the anions order. Relaxed samples remain metallic and eventually become superconducting below about 1 K. Thus, great care was taken in all experiments on (TMTSF)<sub>2</sub>ClO<sub>4</sub> to ensure reproducible cooling of the sample. Indeed, all of the data presented in this chapter were obtained for samples cooled at rates between 0.01 and 0.1 K/min from 32 K to 17 K. Even for these slow cooling rates, subtle differences are found in the data for different cooling rates.

Figure 1.2 shows changes in the microwave loss measured in a cylindrical TE<sub>011</sub> ( $f_{011} = 52.1$  GHz) cavity containing a single (TMTSF)<sub>2</sub>ClO<sub>4</sub> crystal at a temperature of 2.0 K; the frequency is 52.1 GHz in (a) and 75.5 GHz in (b) and (c). The sample was positioned so that the  $c^*$ -axis conductivity dominates the losses in the cavity arising from the perturbation due to the sample [60]. The  $c^*$ -axis conductivity is sufficiently low and the sample sufficiently thin so that microwave-induced  $c^*$ -axis currents penetrate more-or-less uniformly throughout the sample (depolarization regime). In this regime, the loss arising due to the sample is proportional to the conductivity [70–72]. Therefore, one can equivalently consider the vertical axis in Fig. 1.2 to represent AC conductivity. In Fig. 1.2(a), data are plotted (offset) as a function of the orientation of the applied magnetic field within the  $b'c^*$ -plane, for several applied field strengths. In Figs. 1.2(b) and (c), data are plotted (offset) as a function of the field strength, for many field orientations.

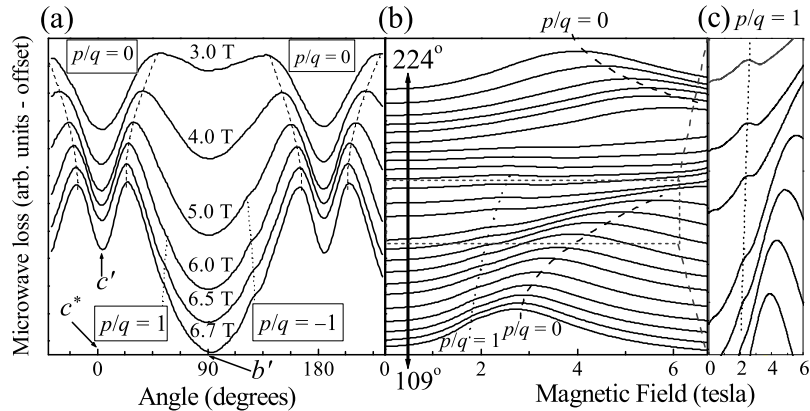


**Fig. 1.2.** Angle- (a) and field-swept [(b) and (c)] microwave absorption data ( $\propto \sigma_{zz}$ ) for  $(\text{TMTSF})_2\text{ClO}_4$  (sample C) [55]. The peaks correspond to POR (offset for clarity), which have been labeled according to the scheme described in the main text. The field was rotated in the  $b'c^*$ -plane; the temperature was 2 K, and the frequency was 52.1 GHz in (a) and 75.5 GHz in (b) and (c). The angle step in (b) is  $5^\circ$ , and the data in (c) correspond to an enlargement of the small resonances denoted as  $p/q = 1$  in (b).

The first thing to note is the resemblance of the data in Fig. 1.2(a) to DC AMRO data, albeit inverted (conductivity rather than resistivity is plotted). Indeed, the quality of the data are comparable to the best AMRO measurements [25], even though the present technique is contactless and extremely sensitive to the mechanical stability of the instrumentation. Clear conductivity resonances (resistance minima) are seen either side of the positions close to  $0^\circ$  and  $180^\circ$  (labeled  $p/q = 0$  and marked by dashed lines); the absolute conductivity is minimum (resistance maximum) close to  $90^\circ$ . Less obvious are weak conductivity resonances (labeled  $p/q = \pm 1$  and marked by dotted lines) superimposed on the sloping background associated with  $p/q = 0$  resonances. The most striking aspect of all of these resonances is the fact that their positions depend on the magnetic field strength, i.e. they do not occur at fixed field orientations (magic angles). This result is quite different from the DC limit, where AMRO minima are always observed at the same field orientations for any field strength. Nevertheless, as we will now explain, the trends observed here at high-frequency are entirely consistent with Eqs. 1.6-1.9.

In order to better understand the general form of the data in Fig. 1.2(a), it is important to first calibrate the field orientation relative to the crystallographic axes. Separate measurements to higher magnetic fields (not shown, see [55]) reveal clear features associated with the field-induced-spin-density-

wave (FISDW) transition. These features scale in field as  $1/\cos\theta$  [75] and do not shift with frequency;  $\theta$  is the angle between the applied field and the crystallographic  $c^*$  direction. In this way, one can identify the principal symmetry directions, and these are indicated in Fig. 1.2(a).

*Conductivity maxima (resonances).* The  $c^*$ -axis conductivity ( $\sigma_{zz}$ ) is dominated by hopping in the  $c$  direction, i.e.  $p = 0$  and  $q = 1$ , or  $p/q = 0$  (see Fig. 1.1). In low-field  $c^*$ -axis DC ( $\omega = 0$ ) AMRO measurements, the deepest resistance minima ( $\sigma_{zz}$  maxima) occur when  $\omega_{01} = 0$ , i.e. when  $\theta = \theta_{01}$  or, equivalently, when the field is directed along the appropriate FS warping direction (see Fig. 1.1(e) and [25]), which is  $c'$  ( $R_{01}$ ) in this case [projection of  $c$  onto the FS ( $b'c^*$ -plane)]. Here, we see in fact that  $\sigma_{zz}$  resonances *do not* occur when the field is directed along  $c'$ . This is due to the finite measurement frequency (denominator in Eq. 1.8). One instead sees resonances when  $\omega_{01} = \pm\omega$ , i.e. either side of  $c'$  at angles given by Eq. 1.9. Nevertheless, in the high-field limit  $\omega_{01}^{max} \gg \omega$  ( $\omega/\omega_{01}^{max} \rightarrow 0$ ), the resonance condition reverts to the DC result. This is apparent in Fig. 1.2(a) where one sees that the two main conductivity peaks move together with increasing field such that they should eventually superimpose at  $\theta = \theta_{01} (\equiv c')$  in the infinite field limit (see also Fig. 1.3 below). In addition to the  $p/q = 0$  resonances, weaker  $p/q = \pm 1$  resonances can be seen either side of  $90^\circ$ .

*Conductivity minima.* The  $c^*$ -axis conductivity should be minimum when  $|\omega - \omega_{01}|$  is maximum (see Eq. 1.8). For  $\omega_{pq}^{max} > \omega > 0$  there are two such directions: (i) when  $\omega_{01} = 0$  ( $\theta = \theta_{01}$ ), corresponding to the field applied along  $c'$ ; and (ii) when  $\omega_{01} = \omega_{01}^{max}$  [ $(\theta - \theta_{01}) = 90^\circ$ ], corresponding to the field directed  $90^\circ$  away from  $c'$  ( $\cong 5^\circ$  away from  $b'$ ). The data in Fig. 1.2(a) show precisely two such minima, with a conductivity resonance in between these directions. For  $\omega > \omega_{pq}^{max}$ , there is no resonance: the conductivity nevertheless exhibits a non-resonant maximum when  $\omega_{01} = \omega_{01}^{max}$  and a minimum when  $\omega_{01} = 0$ , corresponding respectively to the field applied parallel and perpendicular to  $c'$ .

Further evidence that the POR *do not* occur at the magic angles can be seen in Figs. 1.2(b) and (c), where the field strength is varied while its orientation is fixed. Again, one clearly observes a broad peak in  $\sigma_{zz}$  in Fig. 1.2(b) (labeled  $p/q = 0$  and marked by dashed lines) whose position in field shifts upon varying the field orientation. As will be seen below (Fig. 1.3), this conductivity resonance corresponds to precisely the same  $p/q = 0$  resonance observed in Fig. 1.2(a). In fact, closer inspection also reveals clear evidence for the  $p/q = \pm 1$  resonances—see dotted curve and expanded view in Fig. 1.2(c). The very fact that one can observe these resonances without rotating the field indicates that the POR angles change upon varying the magnetic field strength, i.e. the POR (AC AMRO) angles *are not* ‘magic’.

By combining all data obtained from the two methods, one can compile a 2D plot of all POR data (either resonance field versus angle, or resonance angle versus field). In fact, the relevant parameters are the field orientation,  $\theta$ ,

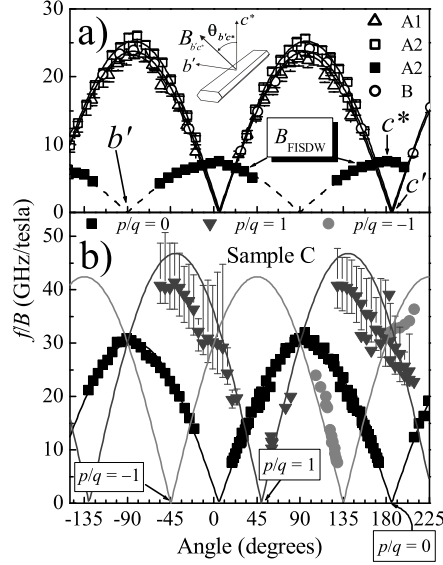


**Fig. 1.3.** Angle dependence of  $f/B$  for (a) samples A and B, and (b) sample C, for field rotation in the  $b'c^*$ -plane; the principal crystal axes are indicated in (a) and the different POR have been labeled in both figures. A1 and A2 denote different cool downs for sample A. The solid curves are fits to Eq. 1.7 (see main text for detailed explanation). In (a), data are also included for the angle dependence of the FISDW transition (solid squares), and the inset depicts the experimental geometry.

and the ratio  $\omega/B$  or  $f/B$ , where  $f$  is the microwave frequency (see Eq. 1.7). Fig. 1.3 displays such 2D plots compiled from data obtained at several frequencies (45 to 76 GHz) for three different samples (A, B, and C); in every case, the field was nominally rotated within the  $b'c^*$ -plane. By plotting data in this way, one can see from Eq. 1.7 that each series of resonances should collapse onto a single sinusoidal arc given by  $A_o \sin |\theta - \theta_{pq}|$ , where the amplitude  $A_o = ev_F R_{pq}/h$  gives a direct measure of the Fermi velocity (provided the  $R_{pq}$  are known). Earlier experiments on samples A and B [Fig. 1.3(a)] were conducted only in the fixed angle, swept field mode, and only  $p/q = 0$  resonances were observed for these samples which were obtained from the same synthesis. As seen in Fig. 1.3(a), to within the experimental error, all of the data for samples A and B collapse onto a single curve. Even data obtained for metallic samples cooled at different rates (A1 and A2) lie on the same curves, in spite of the fact that the POR linewidths differ significantly ( $\tau \sim 1.5 - 7$  ps [76]). Experiments on sample A were conducted in a high-field magnet system, allowing for identification of the FISDW transition (solid data points). The angle-dependence of  $B_{\text{FISDW}}$  was used to confirm

the orientation of the sample [55]. Using the accepted value,  $R_{01} = 13.1 \text{ \AA}$ , and the value for  $A_o$  ( $= 24 \pm 1 \text{ GHz/tesla}$ ) deduced from Fig. 1.3(a), a value of  $v_F = 7.6 \pm 0.3 \times 10^4 \text{ m/s}$  was obtained for samples A and B.

The data presented in Fig. 1.3(b) were obtained for a third sample (C) taken from a separate synthesis. When fully relaxed ( $\tau \sim 6 \text{ ps}$ ), this sample *does* show harmonic POR corresponding to  $p/q = \pm 1$  (in addition to  $p/q = 0$ ). Surprisingly, the obtained  $A_o = 30 \pm 1 \text{ GHz/tesla}$  is significantly higher for this sample, giving a value for the Fermi velocity of  $v_F = 9.5 \pm 0.3 \times 10^4 \text{ m/s}$ . Very preliminary studies on yet another sample also yielded similarly high  $A_o$  values [48]. Therefore, it seems that sample quality has a direct influence on the electronic bandwidth. This could be related to the proximity of the SDW phase, as cleaner (more metallic) samples exhibit higher  $v_F$  values (larger bandwidth). There is also an apparent correlation between the higher  $v_F$  samples and the observation of higher harmonic POR. Whether this is due to the longer scattering times, or to differences in electronic structure, is not clear. Interestingly, it has been demonstrated in a separate study that there is a direct correlation between the scattering time,  $\tau$ , and the superconducting  $T_c$ , suggesting unconventional pairing in  $(\text{TMTSF})_2\text{ClO}_4$  [76].

The solid curves in Fig. 1.3(b) were generated using Eq. 1.7 in the following way: the value of  $A_o$ , and the  $b'$  and  $c'$  directions were determined on the basis of fits to the  $p/q = 0$  POR data (solid squares); the lighter colored curves corresponding to the  $p/q = \pm 1$  POR were then simulated simply by replacing  $R_{pq}$  and  $\theta_{pq}$  with the appropriate (published [4]) values in Eq. 1.7. As can be seen, the agreement is rather good, especially at higher fields (smaller  $f/B$ ). The error bars increase for the weaker  $p/q = \pm 1$  POR at the highest  $f/B$  values because the absolute uncertainty in determining their location is relatively field independent (even increasing slightly with decreasing field). The discrepancy at low fields between the harmonic POR and the simulations could also indicate a possible field dependence of the electronic bandwidth ( $v_F$ ). However, this discrepancy is barely outside of the accuracy of the measurement.

Each POR harmonic observed in Figs. 1.2 and 1.3(b) arises from a particular tight-binding transfer integral  $t_{pq}$ . The relative amplitudes of each of the POR harmonics are related directly to these integrals through the coefficients,  $A_{ii}^{pq}$  ( $\propto t_{pq}^2$ ), in Eq. 1.8. The  $t_{pq}$  affect the nature of the FS warping (Eq. 1.5) which, in turn, influences the tendency of the FS to nest. A higher harmonic content to the FS warping tends to suppress density-wave instabilities. Once again, the general trends observed in these experiments agree with other experimental observations, namely that the more metallic samples exhibit higher harmonic POR (higher harmonic FS warping). Nevertheless, it is quite clear from these measurements that interlayer hopping ( $q = 1$ ) to the nearest-neighbor ( $p = 0$ ) sites is considerably stronger than hopping to next-nearest-neighbor ( $p = -1$ ) and 3<sup>rd</sup>-nearest neighbor ( $p = +1$ ) sites—see Figs. 1.1 and 1.2. In the following section, we present contrasting data for a

system showing very high harmonic POR content. Due to the significantly higher conductivity in  $(\text{TMTSF})_2\text{ClO}_4$  along the  $b'$  direction, it has not been possible to observe  $q = 0$  POR.

There are some important differences between the  $\sigma_{zz}$  POR data displayed in Fig. 1.2 and published DC AMRO data for  $(\text{TMTSF})_2\text{ClO}_4$  [25]. In the present work, POR are observed in the  $\omega \rightarrow 0$  limit when the field is along  $c'$  ( $p/q = 0$ ) and roughly  $\pm 45^\circ$  away from  $c'$  ( $p/q = \mp 1$ ). DC measurements reveal very clear evidence for higher harmonic AMRO such as  $p/q = \pm 2$  and  $\pm 3$ . However, these are only seen in regions of parameter space that were inaccessible with the instrumentation used for the microwave measurements. Comparisons of interlayer ( $q = 1$ ) POR and AMRO data obtained over comparable temperature, field and field orientation ranges reveal similar behaviors in terms of the relative strengths of the  $p/q = 0$  and  $\pm 1$  resonances. However, a surprising aspect of the DC AMRO measurements is a strong, sharp  $q = 0$  ( $p/q = \infty$ ) resonance when the field is parallel to  $b'$  [25], though this dip is less obvious in separate earlier studies [22]. There is no evidence for such a resonance in the microwave measurements. The reason for this difference is not entirely clear. According to Eq. 1.8,  $\sigma_{zz}$  should not exhibit any  $q = 0$  resonances, since  $A_{zz}^{pq} = 0$  for  $q = 0$ . One possibility may be that the DC  $\sigma_{zz}$  measurements are contaminated with  $\sigma_{yy}$ , which should display a dominant  $p/q = \infty$  resonance. However, this may suggest additional (perhaps non-classical) effects in the DC conductivity which do not influence the microwave conductivity [61].

### 1.3.2 $\alpha$ -(BEDT-TTF) $_2$ KHg(SCN) $_4$

Like the Bechgaard salts, the Q2D  $\alpha$ -(BEDT-TTF) $_2$ MHg(SCN) $_4$  ( $M = \text{NH}_4$ , K, Tl, Rb) family of organic charge-transfer salts have a rich history in terms of studies of their Fermiology [4, 7, 8, 10, 21, 30–32, 34–36, 41, 42, 47]. Indeed, the first CR studies were performed on the  $M = \text{K}$  member of this family [30], which is also the focus of the present section. For this compound, the least conducting ( $z$ -) direction is parallel to the crystallographic  $b^*$ -axis [4, 77]. Meanwhile, the conductivity within the  $ac$ -plane ( $\perp b^*$ ) is rather more isotropic than the conductivity within the  $ab$ -plane for  $(\text{TMTSF})_2\text{ClO}_4$ . Consequently, the room temperature FS of  $\alpha$ -(BEDT-TTF) $_2$ KHg(SCN) $_4$  has a more two-dimensional character [77, 78], comprising both open (Q1D) and closed (Q2D) pockets (see Fig. 1 in Ref. [47]). At low temperatures, matters are complicated by the fact that  $\alpha$ -(BEDT-TTF) $_2$ KHg(SCN) $_4$  undergoes a charge-density-wave (CDW) transition at 8 K [4, 79], which leads to a reconstruction of the room temperature FS [7, 8, 10, 19, 80]. Unlike the anion ordering in  $(\text{TMTSF})_2\text{ClO}_4$ , the low temperature state in  $\alpha$ -(BEDT-TTF) $_2$ KHg(SCN) $_4$  is not sensitive to the cooling rate through this CDW transition. The precise nature of the reconstructed FS remains controversial. However, it is believed that the open sections nest, and that the closed pockets reconstruct in such a way as to give rise to new open FS sections together

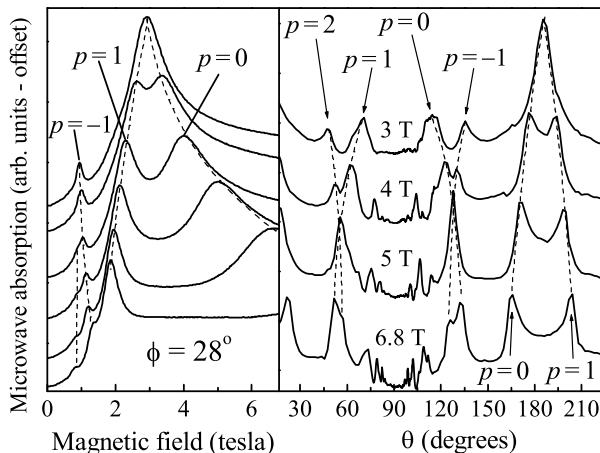


**Fig. 1.4.** Microwave absorption data ( $\propto \sigma_{zz}$ ) for  $\alpha$ -(BEDT-TTF) $_2$ KHg(SCN) $_4$  obtained in (a) field- and (b) angle-swept modes (from [47]). All data were obtained at 2.2 K and 53.9 GHz for field rotation in a plane inclined at  $\phi = 28^\circ$  with respect to the Q1D FS, and the traces have been offset for clarity. The POR, corresponding to peaks in absorption, have been labeled according to the ratio of  $p/q$ .

with smaller closed pockets [19, 80]; one of the original proposals for the reconstructed FS is shown in Fig. 1 of Ref. [47]. This model serves to illustrate most aspects of the POR data presented in this section.

Due to the uncertainty associated with the low temperature FS, several early magneto-optical studies of  $\alpha$ -(BEDT-TTF) $_2$ KHg(SCN) $_4$  incorrectly attributed resonant absorptions to the conventional CR phenomenon [30, 31]. The first indications that they were in fact due to open orbit POR came from angle-dependent cavity perturbation measurements by Ardavan et al. [41]. In these investigations, the applied magnetic field was rotated in two different planes perpendicular to the highly conducting  $ac$ -plane, which is easily identified from the plate-like shape of a typical single crystal. In the case of Q2D CR, the cyclotron frequency depends only on the magnitude of the field component perpendicular to the conducting layers and should, therefore, be insensitive to the particular plane of rotation [35]. The main clue that the resonances observed in  $\alpha$ -(BEDT-TTF) $_2$ KHg(SCN) $_4$  were due to Q1D POR came from the fact that the angle dependence varied strongly with the plane of rotation [36]. In this study, Ardavan et al., were able to fit data corresponding to two FS warping components to sinusoidal arcs of the form given by Eq. 1.7 [41].

Improvements in spectrometer design (enhanced sensitivity and mechanical stability [73, 74]) have since enabled cavity perturbation measurements

with improved signal-to-noise characteristics. Fig. 1.4 displays microwave loss data obtained by Kovalev et al. [47] at 2.2 K and 53.9 GHz, both in field-swept (a) and angle-swept (b) mode. Similar to  $(\text{TMTSF})_2\text{ClO}_4$ , the sample was positioned within the cavity so as to excite interlayer ( $b^*$ -axis) currents throughout the bulk of the sample [60]. Thus, the vertical scale in Fig. 1.4 is proportional to  $\sigma_{zz}$ . Unlike  $(\text{TMTSF})_2\text{ClO}_4$ , however, the reduced in-plane anisotropy, together with the 8 K FS reconstruction, make it impossible to visually identify the orientation of the open FS associated with the low-temperature state. Consequently, one does not initially know the relative angle between the field rotation plane and the Q1D FS ( $xz$ -plane). It is therefore necessary to extend the theory developed in section 1.2.1 for arbitrary rotations [47], i.e. not just rotations within the plane of the FS. Before doing so, however, we present a detailed discussion of the data in Fig. 1.4.

The first point to note upon comparison with Fig. 1.2 is the significant increase in the harmonic content of the POR for  $\alpha$ - $(\text{BEDT-TTF})_2\text{KHg}(\text{SCN})_4$ . This is particularly apparent from the angle-swept data. Indeed, careful inspection of Fig. 1.4(b) reveals over 17 clear resonances within a  $180^\circ$  angle range, along with an apparent continuum of peaks as the field orientation approaches  $90^\circ$  ( $\perp$  to  $b^*$ ); several of these peaks have been labeled. This behavior is dramatically different from that observed for  $(\text{TMTSF})_2\text{ClO}_4$ , and is indicative of a high harmonic content to the FS warping [21]. However, it is not unexpected, as DC AMRO data are equally rich [8]. As will be seen below, this behavior is related to the intrinsic quasi-two-dimensionality of this BEDT-TTF compound, along with the 8 K CDW transition and the resulting FS reconstruction [19, 80].

There are certain similarities between Fig. 1.2(a) and Fig. 1.4(b), but also some key differences. First of all, both figures exhibit a broad conductivity minimum when the applied field is perpendicular to the least conducting direction ( $90^\circ$ ). Furthermore, the POR patterns for both materials exhibit symmetry about  $\theta = 90^\circ$ . In contrast, the behavior around (or close to)  $\theta = 0^\circ$  and  $180^\circ$  is quite different for the two materials. As can be seen from Fig. 1.2(a), the two  $p/q = 0$  resonances either side of  $\theta = 0$  diverge as  $B \rightarrow 0$  ( $\omega \gg \omega_{01}$  limit), whereas they appear to merge together in the high field ( $\omega/\omega_{01} \rightarrow 0$ ) limit, suggesting that the warping direction in  $(\text{TMTSF})_2\text{ClO}_4$  is along  $c'$  ( $5^\circ$  away from  $c^*$ ); in other words, the relevant warping direction corresponds to nearest-neighbor interlayer hopping. By contrast, the two peaks seen in Fig. 1.4(b) merge at 3T. In fact, these two peaks do not even correspond to the same POR harmonic. If one looks carefully at the labeling in Fig. 1.4(b) (*vide infra*), it is apparent that the  $p/q = 0$  peaks will merge somewhere around  $\theta = 150^\circ$ . This implies that the relevant  $R_{01}$  tight-binding hopping direction possesses a significant in-plane component. We note that none of the observed POR have a  $\omega/\omega_{pq} \rightarrow 0$  intercept anywhere close to  $\theta = 0$ , implying that all relevant interlayer hopping matrix elements possess significant in-plane components. Even though  $\alpha$ - $(\text{BEDT-TTF})_2\text{KHg}(\text{SCN})_4$



possesses a low-symmetry triclinic ( $P\bar{1}$ ) structure, this degree of obliqueness of the  $R_{pq}$  vectors *cannot* be explained from high temperature (104 K) crystallographic data [77]. We shall discuss this point further below, along with the observation that the POR imply a very weak decay of the  $t_{pq}$  with increasing  $|p|$ .

As discussed above, before we can fit the POR peak positions to the model developed in section 1.2.1, we must modify Eq. 1.7 slightly for an arbitrary plane of rotation of the applied field. We also adapt this equation and Eq. 1.6 so that they are appropriate for the  $\alpha$ -(BEDT-TTF)<sub>2</sub>KHg(SCN)<sub>4</sub> crystal structure [see Fig. 1.1(e)], for which  $b^*$  corresponds to the least conducting  $z$ -direction. For field rotation in a plane inclined at an angle  $\phi$  with respect to the FS ( $yz$ -plane), the DC AMRO condition is given by,

$$\tan \theta_{pq} = \frac{1}{\cos \phi} \left[ \frac{pl}{qb^*} + \frac{l'}{b^*} \right], \quad (1.10)$$

where, as usual, the angles  $\theta_{pq}$  are measured relative to the  $z$ -axis (see also Fig. 1.1(e) for a definition of the parameters  $l$  and  $l'$ ). The modified resonance condition is then given by the following expression:

$$\frac{\omega_{pq}}{B \cos \theta} = \frac{v_F e b^*}{\hbar} \cos \phi |\tan \theta_{pq} - \tan \theta|. \quad (1.11)$$

From Eq. 1.11 it can be seen that plots of  $f/B \cos \theta$  versus  $\tan \theta \cos \phi$  should produce straight lines with slope  $\pm e b^* v_F / \hbar$ , with offsets given by  $\theta_{pq}$ . Such a plot is shown in Fig. 1.5 for data obtained for two planes of rotation ( $\phi = 28^\circ$  and  $\phi = 66^\circ$ ). As can clearly be seen, the data scale well, particularly in the lower central portion of the plot corresponding to field orientations well away from  $\theta = 90^\circ$ . These results therefore confirm the Q1D nature of the POR, as previously reported by Ardavan et al. [41]. The solid lines represent the best fit to the data with  $v_F$ ,  $l$  and  $l'$  as the only free parameters. The ratios  $l/b^* = 1.2$  and  $l'/b^* = 0.5$  are in excellent agreement with DC AMRO measurements [81–83]. The obtained value of  $v_F = 6.5 \times 10^4$  m/s, meanwhile, cannot be deduced from DC AMRO measurements. The deviation between the data and the fit in the peripheral regions of Fig. 1.5 may have several explanations. First of all, errors in the calibration of the field orientation will be amplified for small values of  $\cos \theta$  and large values of  $\tan \theta$ . It is also likely that the above theory breaks down when the field is oriented close to the direction perpendicular to the plane of the Q1D FS (small  $\cos \theta$ ,  $\cos \phi$  and large  $\tan \theta$ ) due to the Q2D nature of  $\alpha$ -(BEDT-TTF)<sub>2</sub>KHg(SCN)<sub>4</sub>, i.e. one can no longer assume that  $v_x$  is a constant of the motion, resulting in non-separability of all three velocity components. One may estimate an effective mass associated with the high temperature Q2D FS from the obtained value of  $v_F$ . However, such a procedure involves making assumptions about the energy dispersion. Nevertheless, the obtained effective mass ( $m^* = 1.6 - 2.4m_e$ , depending on the assumption made about the energy dispersion) is

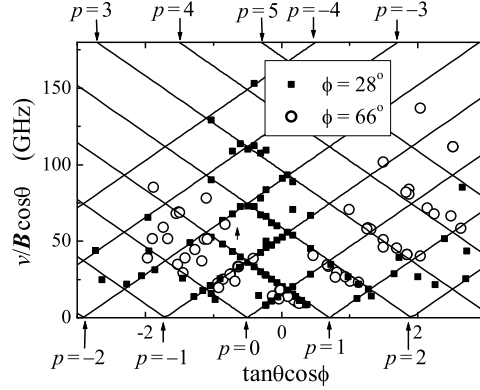


**Fig. 1.5.** A compilation of all data obtained for  $\alpha$ -(BEDT-TTF) $_2$ KHg(SCN) $_4$  scaled according to Eq. 1.11 (from [47]). Several branches have been labeled with the appropriate index  $p$ .

in reasonable agreement with SdH and dHvA measurements [8] (see [47] for a more in depth discussion).

We end this section with a discussion of the very high harmonic content of the POR observed for  $\alpha$ -(BEDT-TTF) $_2$ KHg(SCN) $_4$ . If one takes the view that each resonance corresponds to a given tight-binding transfer integral, then the present study (as well as DC AMRO measurements [8, 21]) would imply a very weak decay of the  $t_{pq}$  with increasing  $|p|$  (for  $q = 1$ ). Such a result would not justify the use of a tight-binding approximation, as it would imply significant orbital overlap to next-nearest and next-next-nearest, etc. sites in the lattice [see Fig. 1.1(e)]. However, as pointed out by Blundell et al. [21], such a view is inappropriate for the low-temperature FS in  $\alpha$ -(BEDT-TTF) $_2$ KHg(SCN) $_4$  due to the 8 K reconstruction that results from the CDW superstructure [19, 80]. The more appropriate view to take is that each POR harmonic corresponds to a Fourier component of the warping of the Q1D FS. Interestingly, inspection of Fig. 1.4 reveals similar amplitudes for the  $p = 0$  and 1 POR, which have similar  $|R_{pq}|$  (they differ in amplitude by less than 10%); the same is true for the  $p = 2$  and  $-1$  POR, for which  $|R_{21}|$  and  $|R_{-11}|$  differ by less than 7%. Thus, it would appear as though the POR intensities scale as some power law of the associated  $R_{pq}$  ( $\propto b^*/|\cos \theta_{pq}|$ ). Meanwhile, the corresponding Fourier amplitudes,  $t_{pq}$ , scale as the square root of the POR intensities, i.e.  $A_{zz}^{pq} \propto t_{pq}^2$ , see Eq. 1.8. We note that for the most extreme anharmonicity, the top hat (or square wave) function, the  $t_{pq}$  should scale as  $R_{pq}^{-1}$  and the POR intensities as  $R_{pq}^{-2}$ :  $R_{01}$  and  $R_{21}$  differ by roughly a factor of 2 [ $(R_{01}/R_{21})^2 = 4$ ], while the corresponding  $p/q = 0$  and  $p/q = 2$  POR differ in intensity by about a factor of 6. Thus, the POR intensities imply

an extremely high harmonic content to the FS warping, which can only be explained in terms of a reconstruction. It is also clear that the  $\mathbf{R}_{pq}$  bear no simple relationship with the principal lattice vectors. Again, this is because the corrugations on the reconstructed FS are related to the CDW nesting vector, not the underlying lattice structure. Therefore, POR measurements are entirely consistent with proposed models for the low-temperature Fermi surface of  $\alpha$ -(BEDT-TTF)<sub>2</sub>KHg(SCN)<sub>4</sub> [19, 80].

#### 1.4 Open-orbit POR in a Q2D system

We conclude this experimental survey by describing a new open-orbit POR effect which was recently reported by Kovalev et al. in the Q2D organic conductor  $\kappa$ -(BEDT-TTF)<sub>2</sub>I<sub>3</sub> [49]. The new effect is observed when the magnetic field is applied parallel to the highly conducting layers—the  $bc$ -plane for this particular compound. As before, the Lorentz force induces periodic quasiparticle trajectories on the warped FS such that  $\dot{\mathbf{k}}$  is perpendicular to the applied field. However, in this case, the FS is a warped cylinder, as depicted in Fig. 1.6(a). Nonetheless, because the FS is warped (finite dispersion along  $a$ ), the Lorentz force leads to periodic modulations of the interlayer quasiparticle velocities,  $v_z$ , which in turn give rise to resonant contributions to  $\sigma_{zz}$  (see Eq. 1.3). As can be seen from Fig. 1.6(a), a range of different trajectories are induced: open-orbits, self-crossing orbits and closed orbits [10, 84–86]. Furthermore, since  $\dot{\mathbf{k}}$  is proportional to  $(\mathbf{v}_F \times \mathbf{B})$ , it is apparent that the periodicities associated with each orbit will vary significantly over the FS, i.e. the POR frequencies associated with different states on the FS are not discrete, as was the case in the previous examples. The DC  $\sigma_{zz}$  (AMRO) is believed to be dominated by the self-crossing orbits, though this has been the subject of some debate [84, 85].

The situation at microwave frequencies is considerably simpler (provided  $\omega\tau > 1$ ). As illustrated in Fig. 1.6(b),  $\sigma_{zz}(\omega)$  exhibits a peak (quasi-resonance) which is dominated by contributions from quasiparticle states corresponding to vertical (symmetry equivalent) strips of the FS which are tangent to the applied field, as depicted in the inset to Fig. 1.6(b). The reason for the dominance of these trajectories is two-fold. First of all, every periodic trajectory has an associated frequency  $\omega_c(\mathbf{k})$ . However, these frequencies vary from zero (smallest closed orbits) up to a maximum cut-off frequency,  $\omega_c^{max}$ , given by the maximum value of  $|(\mathbf{v}_F \times \mathbf{B})|$ . This cut-off gives rise to a singularity in  $\sigma_{zz}(\omega)$ . Note that  $\omega_c^{max}$  corresponds to states with  $\mathbf{v}_F \perp \mathbf{B}$ , i.e. states on FS sections which are tangent to  $\mathbf{B}$ . Second, the density of momentum states diverges at the cut-off frequency, i.e. the number of states per unit frequency range diverges for the tangential patches. The resultant conductivity is obtained by integration over all states on the FS (or all frequencies from 0 to  $\omega_c^{max}$ ). As illustrated in Fig. 1.6(b), such an integration gives rise to a conductivity resonance. The actual value of  $\omega_c^{max}$  ( $= eBav_F/\hbar$ , where  $a$

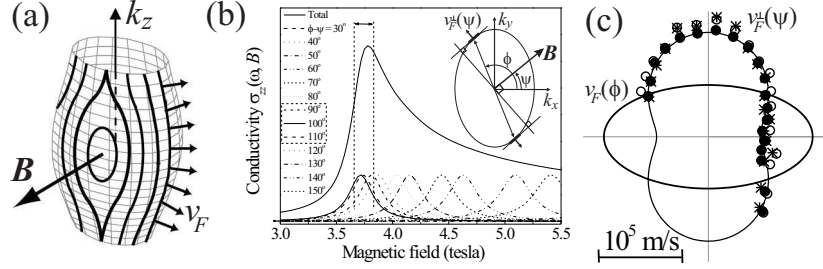


**Fig. 1.6.** (a) An illustration of the quasiparticle trajectories on a warped Q2D FS cylinder for a field oriented perpendicular to the cylinder axis. The resulting trajectories lead to  $v_z$  oscillations and to a resonance in  $\sigma_{zz}$  (see main text). The solid curve in (b) illustrates the conductivity resonance resulting from the electron trajectories in (a). Different parts of the FS contribute to different parts of the resonance (dashed curves). However, the density of resonances is highest for FS patches which are parallel to the applied field (see inset). Consequently, these FS regions dominate the POR. In (c), experimental data are plotted corresponding to  $v_F^\perp$  obtained by various different methods (see [49] for explanation); the dashed curve is a fit to the data and the solid curve represents the corresponding  $v_F^\perp(\phi)$ .

is the interlayer spacing and  $v_F^\perp$  is the Fermi velocity associated with the tangential patches) corresponds to the point on the curve having the maximum slope, i.e. slightly to the low-field side of the peak in  $\sigma_{zz}(B)$ . Measurement of  $\omega_c^{max}$  as a function of the field orientation  $\psi$  within the  $xy$ -plane yields a plot of  $v_F^\perp(\psi)$ . The procedure for mapping  $v_F^\perp(\phi)$  is then identical to that of reconstructing the FS of a Q2D conductor from the measured periods of Yamaji oscillations [4, 87] (see [49] for more in-depth discussion).

Actual experimental data corresponding to  $v_F^\perp(\psi)$ , along with the deduced  $v_F^\perp(\phi)$ , are displayed in Fig. 1.6(c). As with all of the previous POR investigations, a cavity perturbation technique was employed in such a way as to excite only interlayer currents [60, 73]. The interlayer ( $a$ ) direction is easily identified due to the platelet shape of a typical  $\kappa$ -(BEDT-TTF)<sub>2</sub>I<sub>3</sub> single-crystal. Experiments were performed at 4.5 K (above the superconducting transition temperature of 3.5 K) and at a frequency of 53.9 GHz, corresponding to the TE<sub>011</sub> mode of the employed cavity. Use of both the transmitted phase and amplitude enabled precise determination of  $\omega_c^{max}(\phi)$  (see [49] for representative spectra) and the scattering time  $\tau$  ( $= 5$  ps). The FS of  $\kappa$ -(BEDT-TTF)<sub>2</sub>I<sub>3</sub> consists of a network of overlapping weakly warped cylinders. The underlying lattice periodicity results in a removal of the degeneracies at the intersections of these cylinders, giving rise to the coexistence of smaller closed surfaces and open sheets. The deduced anisotropy in  $v_F^\perp(\phi)$  is

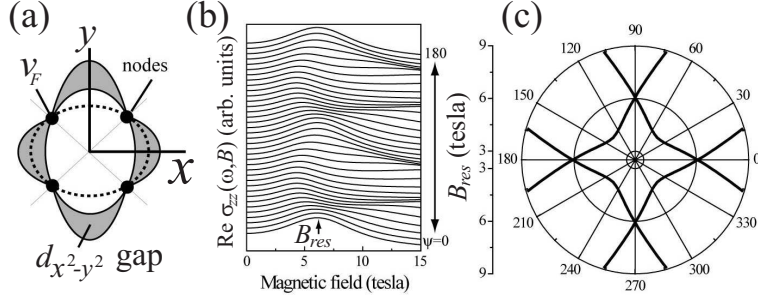


**Fig. 1.7.** (a) Fermi surface and gap for a  $d_{x^2-y^2}$  superconductor, along with (b) the corresponding calculation of the interlayer AC conductivity,  $\sigma_{zz}(\psi, B)$ , and (c) the angle dependence of the resulting resonance fields,  $B_{res}$  (from [54]). Because of the assumption to count only the contribution from normal quasiparticles at the nodes, a discrete  $v_F(\phi)$  was considered (see [54] for further details).

in good agreement with the known anisotropy associated with small Q2D FS for  $\kappa$ -(BEDT-TTF)<sub>2</sub>I<sub>3</sub> [88], i.e.  $v_F^x = 1.3 \times 10^5$  m/s and  $v_F^y = 0.6 \times 10^5$  m/s. Furthermore, one can estimate the effective mass associated with this Q2D pocket using the relation  $m^* = \hbar(S_k/S_v)^{1/2}$ , where  $S_k$  is the cross sectional area of the FS in  $k$ -space and  $S_v$  the area enclosed by  $v_F^\perp(\phi)$  in 2D velocity space. This procedure gives  $m^* = 1.7m_e$  [49], while the experimental value deduced from SdH and dHvA measurements is  $\sim 1.9m_e$  [89].

#### 1.4.1 POR in Q2D nodal superconductors

In the case of the high- $T_c$  superconductors and other candidate Q2D  $d$ -wave superconductors (including several organic conductors [90]), it is generally accepted that normal quasiparticles coexist with the superfluid along vertical line-nodes on the original approximately cylindrical high-temperature FS [91] (see Fig. 1.7). These quasiparticles will dominate the low temperature low-energy electrodynamics, including the microwave spectral range (all other single-particle excitations are gapped) [92–94]. A magnetic field applied parallel to the  $xy$ -plane [ $B(\psi)$ ] preserves in-plane momentum. Consequently, such a field will tend to drive quasiparticles along the vertical line nodes, thus preserving the open orbit POR effect described above. What is more, the nodal quasiparticles will tend to be even longer lived than in the normal state due to the reduced phase space for scattering [92]. Therefore, this dominance of the nodal regions of the FS suggests that it may be possible to directly probe quasiparticles in nodal superconductors via open-orbit POR.

Fig. 1.7(a) illustrates the situation discussed above for a system with a warped elliptical FS (only the cross-section is shown), such as  $\kappa$ -(BEDT-TTF)<sub>2</sub>X (X=I<sub>3</sub>, Cu(NCS)<sub>2</sub>, etc. [4]), with a  $d_{x^2-y^2}$  superconducting gap (shaded area); the dashed curve represents the corresponding angle-dependent

Fermi velocity,  $v_F$ . Within the superconducting state, the FS is gapped everywhere, apart from at the locations of the four line nodes. Fig. 1.7(b) shows numerical simulations of the field dependent interlayer ( $z$ -axis) conductivity,  $\sigma_{zz}(\psi, B)$ , for different field orientations, due to the quasiparticles existing at the line nodes; refer to [54] for further details of these calculations. The peaks in conductivity correspond to the open-orbit POR described in the previous section. However, the angle-dependence is now dominated by the line nodes, rather than the extremal regions of the FS. Thus, the conductivity exhibits two resonances corresponding to pairs of line-nodes on opposite sides of the FS. The resonance field  $B_{res}(\psi)$  depends simply on the angle between the applied field and the lines joining these line-node pairs—hence the two resonances. As shown in Fig. 1.7(c),  $B_{res}(\psi)$  exhibits a four-fold symmetry characteristic of the  $d_{x^2-y^2}$  gap, as opposed to the two fold symmetry characteristic of the original un-gapped elliptical FS [Fig. 1.6(c)].

In principle, one could apply this POR technique to any nodal superconductors which satisfy  $\omega\tau > 1$ . Using this method, it may be possible to measure both  $v_F$  (effective mass) and  $\tau$  associated with nodal quasiparticles. Moreover, it may also be able to confirm the symmetry of the superconducting gap from the angle-dependence of the POR. The organic superconductors may be particularly attractive for such investigations due to their extreme purity. However, recent experiments suggest that it may also be possible to observe this effect in very pure high- $T_c$  compounds such as  $Y_2Ba_2Cu_3O_{6+x}$  [94] and  $Tl_2Ba_2CuO_{6+\delta}$  [58].

## 1.5 Discussion and comparisons with other experiments

The first four columns in Table 1.1 summarize optical constants deduced from the POR studies outlined in the previous sections, for: **(1)**  $(TMTSF)_2ClO_4$ ; **(2)**  $\alpha$ -(BEDT-TTF) $_2$ KHg(SCN) $_4$ ; and **(3)**  $\kappa$ -(BEDT-TTF) $_2I_3$ . The final four columns list various physical parameters obtained from the literature; unless otherwise indicated, these parameters represent low-temperature limiting values. The first point to note is that all three materials appear to display coherent 3D band transport at low temperatures. This can be seen by comparing the scattering times (either the transport time,  $\tau$ , or the quantum lifetime,  $\tau_\varphi$ ) with the interlayer hopping times,  $\tau_h$ , i.e. for all materials,  $\tau_h < \{\tau, \tau_\varphi\}$ . However, for all three materials, the difference is not so great (roughly an order of magnitude). Thus, one may expect a crossover to an incoherent regime at fairly low temperatures. For **(3)**, the transport lifetime deduced from the POR measurements is in excellent agreement with the quantum lifetime deduced from dHvA studies [96], in spite of the fact that the samples were grown completely independently by different groups. For **(2)**, meanwhile, there is a significant discrepancy between the transport and quantum lifetimes. Part of the reason for this discrepancy could be related to the complexities of the low

temperature state of  $\alpha$ -(BEDT-TTF)<sub>2</sub>KHg(SCN)<sub>4</sub> [8]. In particular, the reconstructed FS consists of multiply connected Q1D and Q2D sections, giving rise to an extremely rich pattern of quantum oscillations involving magnetic breakdown. It is also notable that the POR data presented in section 1.3.2 clearly originate from quasiparticles belonging to an open FS, whereas quasiparticles responsible for quantum oscillatory phenomena necessarily involve closed orbits. Thus, a direct comparison between  $\tau$  and  $\tau_\varphi$  is probably inappropriate for **(2)**. Nevertheless, a significant (order of magnitude) difference between these quantities has previously been noted for another member (M = NH<sub>4</sub>) of the  $\alpha$ -phase salts, which *does not* undergo a low temperature FS reconstruction [35]. Such a difference can be explained in terms of an inhomogeneous broadening of Landau levels, which would show up in  $\tau_\varphi$ , but not necessarily in the transport lifetime [11]. Due to the absence of closed pockets, a comparison between  $\tau$  and  $\tau_\varphi$  is not possible for **(1)**.

As discussed in section 1.2,  $\omega$  and  $\omega_c$  play essentially the same role in Eq. 1.4. It is, therefore, interesting to compare optical constants obtained from these measurements with published values deduced from more conventional optical methods. There is one caveat, however: most optical reflectivity measurements are limited to frequencies well above the scattering rates ( $\tau^{-1}$ ) deduced from these POR studies. For example, optical studies of **(2)** are lim-

**Table 1.1.** Physical parameters deduced from these investigations and from the literature for: **(1)** (TMTSF)<sub>2</sub>ClO<sub>4</sub>; **(2)**  $\alpha$ -(BEDT-TTF)<sub>2</sub>KHg(SCN)<sub>4</sub>; and **(3)**  $\kappa$ -(BEDT-TTF)<sub>2</sub>I<sub>3</sub>. The transport scattering time ( $\tau$ ) and Fermi velocity ( $v_F$ ) were deduced from POR measurements. The effective masses ( $m^*$ ) for **(2)** and **(3)** were deduced from the obtained values of  $v_F$ , as described in refs [47] and [55], respectively;  $m^*$  for **(1)** was deduced on the basis of a tight binding model, as described in [47]. The quantity  $ne^2\tau/m^*$  represents the DC conductivity deduced on the basis of the  $\tau$  and  $m^*$  values obtained from the POR measurements, using literature values for the carrier concentration  $n$  [4, 77, 95]; we assume that a carrier density corresponding to only 20% of the Brillouin zone contributes to the conductivity in the low-temperature state of **(2)** [8].  $\tau_h$  is the interlayer hopping time deduced from:  $a$ —the interlayer bandwidth [4];  $b$ —Ref. [47],  $c$ —Ref. [96].  $\tau_\varphi$  is the quantum lifetime deduced from magneto oscillation data:  $d$ —Ref. [8],  $e$ —Ref. [96]. The optical scattering time ( $\tau^{opt}$ ) and DC conductivity ( $\sigma_o^{opt}$ ) were taken from Refs. [97, 98] for **(1)** at 10 K, from Ref. [99] for **(2)** at 6 K, and from Ref. [95] for **(3)** at 15 K.

	$\tau$ (ps)	$v_F$ (/10 <sup>4</sup> ms <sup>-1</sup> )	$m^*$ ( $m_e$ )	$ne^2\tau/m^*$ (S cm <sup>-1</sup> )	$\tau_h$ (ps)	$\tau_\varphi$ (ps)	$\tau^{opt}$ (ps)	$\sigma_o^{opt}$ (S cm <sup>-1</sup> )
<b>1.</b>	1-7*	7.6-9.5*	1.45-1.75*	$\sim 10^6$	0.7 <sup>a</sup>	-	> 10	10 <sup>3</sup> -10 <sup>4</sup>
<b>2.</b>	15	6.5	1.6-2.4	$3 \times 10^5$	0.75 <sup>b</sup>	0.8-2.5 <sup>d</sup>	1	$\sim 10^3$
<b>3.</b>	5	10	1.7-2.5	$4 \times 10^5$	1 <sup>c</sup>	5 <sup>e</sup>	$\sim 0.1$	$\sim 1500$

\* cooling rate dependent

ited to frequencies above  $50 \text{ cm}^{-1}$  (1.5 THz) [99], and those of **(3)** to above  $500 \text{ cm}^{-1}$  (15 THz) [95]. Consequently, most of the low-temperature Drude spectral weight does not even contribute to the measured reflectivity in these investigations. The only material for which low-frequency cavity perturbation data do exist (down to  $\sim 5 \text{ cm}^{-1}$ ) is  $(\text{TMTSF})_2\text{ClO}_4$  [97, 98, 100, 101]. Nevertheless, one still has to rely on Kramers-Kronig and Hagen-Rubens extrapolation for  $\omega \rightarrow 0$  in order to recover the Drude spectral weight [68]. Thus, such techniques ultimately rely on accurate measurements of the DC conductivity. It is perhaps not surprising, therefore, that the optical scattering rates,  $\tau^{opt}$ , deduced for **(2)** and **(3)** are roughly half the minimum frequencies employed in the measurement, i.e.  $\sim 30 \text{ cm}^{-1}$  and  $\sim 300 \text{ cm}^{-1}$ , respectively. In both cases, the deduced values of  $\tau^{opt}$  are nowhere near the scattering rates deduced from POR studies. In addition, there is at least a two orders of magnitude difference between the DC conductivities found in optical studies and those deduced from POR measurements which assume a 100% contribution of free carriers to the Drude peak.

For  $(\text{TMTSF})_2\text{ClO}_4$ , the situation is only slightly better. The values for  $\tau^{opt}$  and  $\sigma_o^{opt}$  listed in Table 1.1 were taken from the more recent literature [97, 98]. While the value of  $\tau^{opt}$  is in reasonable agreement with the POR data (because of the lower frequencies employed), the value of  $\sigma_o^{opt}$  clearly is not; again, there is a factor of 100 difference between the upper range for  $\sigma_o^{opt}$  and the POR estimate. However, there exist earlier reports of considerably higher conductivities, including the original study of Bechgaard et al. [102], where low temperature values in the  $10^5 - 10^6 \text{ S cm}^{-1}$  range were found. This agrees nicely with the POR value quoted in Table 1.1. It is notable that, when the larger conductivity is used to extrapolate optical data, an anomalously narrow low-energy Drude peak is obtained (width =  $0.034 \text{ cm}^{-1}$ , or 1 GHz) [101]. This highlights the problems associated with characterization of the low energy Drude spectral weight from conventional broad band optical techniques which are ordinarily limited to frequencies above about  $10 \text{ cm}^{-1}$ . However, several recent studies have suggested a general trend among many of the layered organic conductors: namely, that only a small fraction (as little as 1%) of the overall spectral weight is to be found in the low-energy free carrier (Drude) response. If this is indeed the case, then the DC conductivities deduced from POR measurements should be revised downwards by a factor of 100, bringing them into alignment with the  $\sigma_o^{opt}$  values.

The experimental situation presented above is far from ideal. While the POR measurements give reliable estimates of the quasiparticle scattering time from the resonance half-width, the spectrometer is not calibrated to measure the absolute loss due to the sample. Consequently, the absolute value of the conductivity is not obtained from these measurements. Furthermore, it is usually the interlayer conductivity that is measured, so one has to make the assumption that the measured scattering time is isotropic. Nevertheless, the obtained value of  $\tau$  broadly agrees with other techniques such as SdH and



dHvA. In the case of the optical studies, neither  $\tau^{opt}$  or  $\sigma_o^{opt}$  are obtained directly for the three materials highlighted in this chapter, and the reported  $\tau^{opt}$  values are inconsistent with many other observations, e.g. the dHvA and SdH effects. Nevertheless, it has been suggested that both the Bechgaard and  $\alpha$ -phase BEDT-TTF salts exhibit dramatic deviations from a simple Drude response on the basis of these optical studies [97,99]. One of the main pieces of evidence is the missing spectral weight in the low-energy Drude peak. However, as already pointed out above, if one takes the POR scattering time and the DC conductivity reported by Bechgaard et al. [102], then one finds that the Drude peak in  $(\text{TMTSF})_2\text{ClO}_4$  accounts for 100% of the free-carrier spectral weight. Furthermore, the observation of magneto-oscillatory phenomenon in many of these materials is hard to reconcile with the notion of a Drude peak containing only 1% of the free-carrier spectral weight. Clearly, the only way to resolve these issues is through the development of techniques which accurately measure the low-energy electrodynamic properties (including DC) of these materials. This ought to be a relatively straightforward task, but available samples are often tiny and prone to twinning and micro-cracking, which can severely influence such measurements.

Finally, we note that very extensive low-energy electrodynamic measurements have been reported down to  $0.1 \text{ cm}^{-1}$  for the  $(\text{TMTSF})_2\text{PF}_6$  member of the Bechgaard family [97,98,103], as have detailed AMRO measurements [23]. Furthermore, the low-temperature properties of this material are not influenced by anion ordering. Therefore, it is highly desirable to make POR measurements on  $(\text{TMTSF})_2\text{PF}_6$ . However, this requires the application of hydrostatic pressure ( $> 7 \text{ kbar}$ ) in order to suppress a SDW phase that occurs below 12 K under ambient pressure conditions. We note that such techniques are currently under development.

## 1.6 Summary and conclusions

On the basis of detailed POR measurements, we present compelling evidence that the low-energy magnetoelectrodynamics of three contrasting organic conductors,  $(\text{TMTSF})_2\text{ClO}_4$ ,  $\alpha$ - $(\text{BEDT-TTF})_2\text{KHg}(\text{SCN})_4$  and  $\kappa$ - $(\text{BEDT-TTF})_2\text{I}_3$ , can be explained on the basis of a conventional semiclassical Boltzmann theory, and that all three materials exhibit coherent 3D band transport at liquid helium temperatures. We demonstrate that there is nothing ‘magic’ about the angles at which DC resistance minima are observed in AMRO experiments, findings that do not support the notion of a fundamentally different thermodynamic ground states at, and away from, the Lebed ‘magic angles’. We also argue that the POR can account for 100% of the free-carrier spectral weight for  $(\text{TMTSF})_2\text{ClO}_4$ . Again, this finding appears to conflict with claims of dramatic deviations from a simple Drude response on the basis of broadband optical measurements. Finally, we propose that the POR technique could be used to probe quasiparticles in nodal superconductors.

## 1.7 Acknowledgements

This work was supported by the National Science Foundation (DMR0239481) and by Research Corporation. The authors acknowledge useful discussions with David Tanner, Victor Yakovenko and Martin Dressel.

## References

1. A. W. Overhauser, *Phys. Rev.* **128**, 1437 (1962).
2. S. Kagoshima, H. Nagasawa, and T. Sambogni, *One-dimensional conductors* (Springer-Verlag, Berlin, 1988).
3. G. Grüner, *Density Waves in Solids* (Addison Wesley, Reading, MA, 1994).
4. T. Ishiguro, K. Yamaji, and G. Saito, *Organic Superconductors* (Springer, Heidelberg, Germany, 1998).
5. R. Louati, S. Charfi-Kaddour, A. B. Ali, R. Bennaceur, and M. Héritier, *Phys. Rev. B* **62**, 5957 (2000).
6. Y. Tanuma, K. Kuroki, Y. Tanaka, R. Arita, S. Kashiwaya, and H. Aoki, *Phys. Rev. B* **66**, 094507 (2002).
7. J. Wosnitza, *Fermi Surfaces of Low-dimensional Organic Metals and Superconductors, Springer Tracts in Modern Physics* (Springer-Verlag, Berlin and Heidelberg, 1996).
8. J. Singleton, *Rep. Prog. Phys.* **63**, 1111 (2000).
9. J. Singleton, *Band Theory and Electronic Properties of Solids* (Oxford University Press, Oxford, 2001).
10. M. V. Kartsovnik, *Chem. Rev.* **104**, 5737 (2004).
11. D. Shoenberg, *Magnetic Oscillations in Metals* (Cambridge University press, Cambridge, 1984).
12. A. A. Abrikosov, *Fundamentals of the Theory of Metals* (Elsevier, New York, 1988).
13. A. G. Lebed, *JETP Lett.* **43**, 174 (1986).
14. A. G. Lebed and P. Bak, *Phys. Rev. Lett.* **63**, 1315 (1989).
15. G. S. Boebinger, G. Montambaux, M. L. Kaplan, R. C. Haddon, S. V. Chichester, and L. Y. Chiang, *Phys. Rev. Lett.* **64**, 591 (1990).
16. T. Osada, A. Kawasumi, S. Kagoshima, N. Miura, and G. Saito, *Phys. Rev. Lett.* **66**, 1525 (1991).
17. M. J. Naughton, O. H. Chung, M. Chaparala, X. Bu, and P. Coppens, *Phys. Rev. Lett.* **67**, 3712 (1991).
18. T. Osada, S. Kagoshima, and N. Miura, *Phys. Rev. B* **46**, 1812 (1992).
19. M. V. Kartsovnik, A. E. Kovalev, and N. D. Kusch, *J. Phys. I* **3**, 1187 (1993).
20. G. M. Danner, W. Kang, and P. M. Chaikin, *Phys. Rev. Lett.* **72**, 3714 (1994).
21. S. J. Blundell and J. Singleton, *Phys. Rev. B* **53**, 5609 (1996).
22. E. I. Chashechkina and P. M. Chaikin, *Phys. Rev. B* **56**, 13658 (1997).
23. E. I. Chashechkina and P. M. Chaikin, *Phys. Rev. Lett.* **80**, 2181 (1998).
24. I. J. Lee and M. J. Naughton, *Phys. Rev. B* **58**, R13343 (1998).
25. W. Kang, H. Kang, Y. J. Jo, and S. Uji, *Synth. Met.* **133-134**, 15 (2003).
26. A. G. Lebed, N. N. Bagmet, and M. J. Naughton, *Phys. Rev. Lett.* **93**, 157006 (2004).

27. B. K. Cooper and V. M. Yakovenko, *Phys. Rev. Lett.* **96**, 037001 (2006).
28. F. Zwick, S. Brown, G. Margaritondo, C. Merlic, M. Onellion, J. Voit, and M. Grioni, *Phys. Rev. Lett.* **79**, 3982 (1997).
29. A. S. Perel, J. S. Brooks, C. J. G. N. Langerak, T. J. B. M. Janssen, J. Singleton, J. A. A. J. Perenboom, and L. Y. Chiang, *Phys. Rev. Lett.* **67**, 2072 (1991).
30. J. Singleton, F. L. Pratt, M. Doporto, T. J. B. M. Janssen, M. Kurmoo, J. A. A. J. Perenboom, W. Hayes, and P. Day, *Phys. Rev. Lett.* **68**, 2500 (1992).
31. S. Hill, J. Singleton, F. L. Pratt, M. Doporto, W. Hayes, T. J. B. M. Janssen, J. A. A. J. Perenboom, M. Kurmoo, and P. Day, *Synth. Met.* **56**, 2566 (1993).
32. S. Hill, A. Wittlin, J. van Bentum, J. Singleton, W. Hayes, J. A. A. J. Perenboom, M. Kurmoo, and P. Day, *Synth. Met.* **70**, 821 (1995).
33. S. Hill, P. S. Sandhu, M. Boonman, J. A. A. J. Perenboom, A. Wittlin, S. Uji, J. S. Brooks, R. Kato, H. Sawa, and S. Aonuma, *Phys. Rev. B* **54**, 13536 (1996).
34. A. Polisski, J. Singleton, P. Goy, W. Hayes, M. Kurmoo, and P. Day, *J. Phys. Condens. Matter* **8**, L195 (1996).
35. S. Hill, *Phys. Rev. B* **55**, 4931 (1997).
36. S. J. Blundell, A. Ardavan, and J. Singleton, *Phys. Rev. B* **55**, R6129 (1997).
37. H. Ohta, Y. Yamamoto, K. Akioka, M. Motokawa, T. Sasaki, and T. Fukase, *Synth. Met.* **86**, 2011 (1997).
38. K. Akioka, H. Ohta, Y. Yamamoto, M. Motokawa, and K. Kanoda, *Synth. Met.* **86**, 2051 (1997).
39. H. Ohta, Y. Yamamoto, K. Akioka, M. Motokawa, and K. Kanoda, *Synth. Met.* **86**, 1913 (1997).
40. S. Hill, J. A. A. J. Perenboom, T. Stalcup, N. S. Dalal, T. Hathaway, and J. S. Brooks, *Physica B* **246-247**, 549 (1998).
41. A. Ardavan, J. M. Schrama, S. J. Blundell, J. Singleton, W. Hayes, M. Kurmoo, P. Day, and P. Goy, *Phys. Rev. Lett.* **81**, 713 (1998).
42. A. Ardavan, S. J. Blundell, and J. Singleton, *Phys. Rev. B* **60**, 15500 (1999).
43. C. Palassis, M. Mola, J. Tritz, S. Hill, S. Uji, K. Kawano, M. Tamura, T. Naito, and H. Kobayashi, *Synth. Met.* **120**, 999 (2001).
44. Y. Oshima, N. Nakagawa, K. Akioka, H. Ohta, S. Okubo, M. Tamura, Y. Nishio, and K. Kajita, *Synth. Met.* **103**, 1919 (1999).
45. H. Ohta, Y. Oshima, N. Nakagawa, K. Akioka, S. Okubo, and K. Kanoda, *Synth. Met.* **103**, 1913 (1999).
46. Y. Oshima, H. Ohta, S. Okubo, K. Koyama, M. Motokawa, M. Tamura, Y. Nishio, and K. Kajita, *Synth. Met.* **120**, 853 (2001).
47. A. E. Kovalev, S. Hill, and J. S. Qualls, *Phys. Rev. B* **66**, 134513 (2002).
48. A. Kovalev, S. Hill, S. Takasaki, J. Yamada, and H. Anzai, *J. Appl. Phys.* **93**, 8665 (2003).
49. A. E. Kovalev, S. Hill, K. Kawamo, M. Tamura, T. Naito, and H. Kobayashi, *Phys. Rev. Lett.* **91**, 216402 (2003).
50. Y. Oshima, H. Ohta, K. Koyama, M. Motokawa, H. M. Yamamoto, and R. Kato, *J. Phys. Soc. Jpn.* **71**, 1031 (2002).
51. Y. Oshima, H. Ohta, K. Koyama, M. Motokawa, H. Yamamoto, R. Kato, M. Tamura, Y. Nishino, and K. Kajita, *J. Phys. Soc. Jpn.* **72**, 143 (2003).
52. Y. Oshima, M. Kimata, K. Kishigi, H. Ohta, K. Koyama, M. Motokawa, and H. Nishikawa, *Phys. Rev. B* **68**, 54526 (2003).

53. S. Takahashi, A. E. Kovalev, S. Hill, S. Takasaki, J. Yamada, H. Anzai, J. S. Qualls, K. Kawano, M. Tamura, T. Naito, and H. Kobayashi, *Int. J. Mod. Phys. B* **27-29**, 3499 (2004).
54. S. Takahashi and S. Hill, *J. Appl. Phys.* **97**, 10B106 (2005).
55. S. Takahashi, S. Hill, S. Takasaki, J. Yamada, and H. Anzai, *Phys. Rev. B* **72**, 024540 (2005).
56. A. P. MacKenzie and Y. Maeno, *Rev. Mod. Phys.* **75**, 657 (2003).
57. S. Hill, J. S. Brooks, Z. Q. Mao, and Y. Maeno, *Phys. Rev. Lett.* **84**, 3374 (2000).
58. N. E. Hussey, M. Abdel-Jawad, A. Carrington, A. P. Mackenzie, and L. Balicas, *Nature* **425**, 814 (2003).
59. A. Damasceli, Z. Hussain, and Z.-X. Shen, *Rev. Mod. Phys.* **75**, 437 (2003).
60. S. Hill, *Phys. Rev. B* **62**, 8699 (2000).
61. D. G. Clarke, S. P. Strong, P. M. Chaikin, and E. I. Chashechkina, *Science* **279**, 2071 (1998).
62. W. Wu, I. J. Lee, and P. M. Chaikin, *Phys. Rev. Lett.* **91**, 056601 (2003).
63. W. Wu, P. M. Chaikin, W. Kang, J. Shinagawa, W. Yu, and S. E. Brown, *Phys. Rev. Lett.* **94**, 097004 (2005).
64. E. S. Choi, J. S. Brooks, H. Kang, Y. J. Jo, and W. Kang, *Phys. Rev. Lett.* **95**, 187001 (2005).
65. P. Moses and R. H. McKenzie, *Phys. Rev. B* **60**, 7998 (1999).
66. R. H. McKenzie and P. Moses, *Phys. Rev. B* **60**, 11241 (1999).
67. T. Osada, K. Kobayashi, and E. Ohmichi, *Synth. Met.* **135-136**, 653 (2003).
68. M. Dressel and G. Grüner, *Electrodynamics Of Solids: Optical Properties Of Electrons In Matter* (Cambridge University Press, Cambridge, 2002).
69. M. Dressel, A. Schwartz, G. Grüner, and L. Degiorgi, *Phys. Rev. Lett.* **77**, 398 (1996).
70. O. Klein, S. Donovan, M. Dressel, and G. Grüner, *Int. J. Infrared Millim. Waves* **1993**, 2423 (1993).
71. S. Donovan, O. Klein, M. Dressel, K. Holczer, and G. Grüner, *Int. J. Infrared Millim. Waves* **14**, 2459 (1993).
72. M. Dressel, O. Klein, S. Donovan, and G. Grüner, *Int. J. Infrared Millim. Waves* **14**, 2489 (1993).
73. M. Mola, S. Hill, P. Goy, and M. Gross, *Rev. Sci. Inst.* **71**, 186 (2000).
74. S. Takahashi and S. Hill, *Rev. Sci. Inst.* **76**, 023114 (2005).
75. T. Osada, H. Nose, and M. Karaguchi, *Physica B* **294-295**, 402 (2001).
76. S. Takahashi, S. Hill, S. Takasaki, J. Yamada, and H. Anzai, *AIP conference proceedings* **850**, 619 (2006).
77. H. Mori, S. Tanaka, M. Oshima, G. Saito, T. Mori, Y. Maruyama, and H. Inokuchi, *Bull. Chem. Soc. Jpn.* **63**, 2183 (1990).
78. C. E. Campos, P. S. Sandhu, J. S. Brooks, and T. Ziman, *Phys. Rev. B* **53**, 12725 (1996).
79. N. Harrison, *Phys. Rev. Lett.* **83**, 1395 (1999).
80. N. Harrison, E. Rzepniewski, J. Singleton, P. J. Gee, M. M. Honold, P. Day, and M. Kurmoo, *J. Phys.: Condens. Matter* **11**, 7227 (1999).
81. A. Kovalev, M. Kartsovnik, R. Shibaeva, L. Rozenberg, I. Schegolev, and N. Kushch, *Solid State Commun.* **89**, 575 (1994).
82. Y. Iye, R. Yagi, N. Hanasaki, S. Kagoshima, H. Mori, H. Fujimoto, and G. Saito, *J. Phys. Soc. Jpn.* **63**, 674 (1994).

83. J. Caulfield, S. Blundell, M. du Croo de Jongh, P. Hendriks, J. Singleton, M. Doporto, F. Pratt, A. House, J. Perenboom, W. Hayes, M. Kurmoo, and P. Day, *Phys. Rev. B* **51**, 8325 (1995).
84. N. Hanasaki, S. Kagoshima, T. Hasegawa, T. Osada, and N. Miura, *Phys. Rev. B* **57**, 1336 (1998).
85. V. G. Peschansky and M. V. Kartsovnik, *Phys. Rev. B* **60**, 11207 (1999).
86. J. Singleton, P. A. Goddard, A. Ardavan, N. Harrison, S. J. Blundell, J. A. Schlueter, and A. M. Kini, *Phys. Rev. Lett.* **88**, 037001 (2002).
87. K. Yamaji, *J. Phys. Soc. Jpn.* **58**, 1520 (1989).
88. H. Kobayashi, K. Kawano, T. Naito, and A. Kobayashi, *J. Mater. Chem.* **5**, 1681 (1995).
89. E. Balthes, D. Schweitzer, I. Heinen, H. J. Keller, W. Strunz, W. Biberacher, A. G. M. Jansen, and E. Steep, *Z. Phys. B* **99**, 163 (1996).
90. R. H. McKenzie, *Science* **278**, 820 (1997).
91. C. C. Tsuei and J. R. Kirtley, *Rev. Mod. Phys.* **72**, 969 (2000).
92. A. Hosseini, R. Harris, S. Kamal, P. Dosanjh, J. Preston, R. Liang, W. N. Hardy, and D. A. Bonn, *Phys. Rev. B* **60**, 1349 (1999).
93. J. Corson, J. Orenstein, S. Oh, J. O'Donnell, and J. N. Eckstein, *Phys. Rev. Lett.* **85**, 2569 (2000).
94. P. J. Turner, R. Harris, S. Kamal, M. E. Hayden, D. M. Broun, D. C. Morgan, A. Hosseini, P. Dosanjh, G. K. Mullins, J. S. Preston, R. Liang, D. A. Bonn, and W. N. Hardy, *Phys. Rev. Lett.* **90**, 237005 (2003).
95. M. Tamura, H. Tajima, K. Yakushi, H. Kuroda, A. Kobayashi, R. Kato, and H. Kobayashi, *J. Phys. Soc. Jpn.* **60**, 3861 (1991).
96. J. Wosnitzer, J. Hagel, J. S. Qualls, J. S. Brooks, E. Balthes, D. Schweitzer, J. A. Schlueter, U. Geiser, J. Mohtasham, R. W. Winter, and G. L. Gard, *Phys. Rev. B* **65**, 180506 (2002).
97. A. Schwartz, M. Dressel, G. Gruner, V. Vescoli, L. Degiorgi, and T. Giamarchi, *Phys. Rev. B* **58**, 1261 (1998).
98. M. Dressel, K. Petukhov, B. Salameh, P. Zornoza, and T. Giamarchi, *Phys. Rev. B* **71**, 075104 (2005).
99. M. Dressel, N. Drichko, J. Schlueter, and J. Merino, *Phys. Rev. Lett.* **90**, 167002 (2003).
100. H. K. Ng, T. Timusk, and K. Bechgaard, *J. Phys. Colloq. France* **44**, 867 (1983).
101. N. Cao, T. Timusk, and K. Bechgaard, *J. Phys. I France* **6**, 1719 (1996).
102. K. Bechgaard, K. Carneiro, M. Olson, F. B. Rasmussen, and C. S. Jacobsen, *Phys. Rev. Lett.* **46**, 852 (1981).
103. S. Donovan, Y. Kim, L. Degiorgi, M. Dressel, G. Gruner, and W. Wonneberger, *Phys. Rev. B* **49**, 3363 (1994).